AGU PUBLICATIONS

Water Resources Research

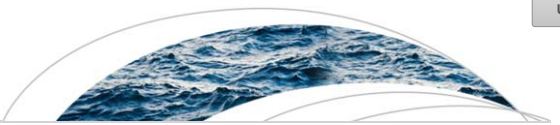

RESEARCH ARTICLE
10.1002/2017WR021646

Key Points:
- A new line laser scanner approach improves bed level monitoring in morphodynamic experiments
- A LOESS fitting algorithm allows to handle outliers and missing data effectively
- The best results are obtained for small flow velocities commonly used in experiments with light-weight sediment

Correspondence to:
T. V. de Ruijsscher,
timo.deruijsscher@wur.nl

Citation:
de Ruijsscher, T. V., Hoitink, A. J. F., Dinnissen, S., Vermeulen, B., & Hazenberg, P. (2018). Application of a line laser scanner for bed form tracking in a laboratory flume. *Water Resources Research*, *54*, 2078–2094. https://doi.org/10.1002/2017WR021646

Received 2 AUG 2017
Accepted 28 FEB 2018
Accepted article online 8 MAR 2018
Published online 23 MAR 2018

Application of a Line Laser Scanner for Bed Form Tracking in a Laboratory Flume

T. V. de Ruijsscher[1], A. J. F. Hoitink[1], S. Dinnissen[1,2], B. Vermeulen[3], and P. Hazenberg[1]

[1]Hydrology and Quantitative Water Management Group, Department of Environmental Sciences, Wageningen University, Wageningen, The Netherlands, [2]Now at Waterschap Hunze en Aa's, The Netherlands, [3]Marine and Fluvial Systems Group, Department of Water Engineering and Management, Faculty of Engineering Technology, University of Twente, The Netherlands

Abstract A new measurement method for continuous detection of bed forms in movable bed laboratory experiments is presented and tested. The device consists of a line laser coupled to a 3-D camera, which makes use of triangulation. This allows to measure bed forms during morphodynamic experiments, without removing the water from the flume. A correction is applied for the effect of laser refraction at the air-water interface. We conclude that the absolute measurement error increases with increasing flow velocity, its standard deviation increases with water depth and flow velocity, and the percentage of missing values increases with water depth. Although 71% of the data is lost in a pilot moving bed experiment with sand, still high agreement between flowing water and dry bed measurements is found when a robust LOcally weighted regrESSion (LOESS) procedure is applied. This is promising for bed form tracking applications in laboratory experiments, especially when lightweight sediments like polystyrene are used, which require smaller flow velocities to achieve dynamic similarity to the prototype. This is confirmed in a moving bed experiment with polystyrene.

1. Introduction

In fluvial and tidal systems, bed forms like ripples, dunes and bars interact with the flow (Allen, 1984; Seminara, 2010). To study the mechanisms causing these interactions in a laboratory setting, measurement devices should ideally not disturb the experiment and monitor the relevant physical parameters continuously, from the start of the experiment onward.

Nowadays, numerical models are used extensively in hydro- and morphodynamic studies, ranging from large-scale parametrized hydro- and morphodynamic models (e.g., Lesser et al., 2004; Struiksma, 1985) to more detailed process-based models for sediment sorting (Blom, 2008) and particle-based sediment transport (Nabi et al., 2013a, 2013b). The predictive capabilities of morphodynamic models, however, remain highly limited to date. Because of the limitations of numerical methods to simulate morphodynamics, laboratory experiments remain important, both to gain insight in physical mechanisms and to validate numerical models. To study the development and evolution of bed forms, continuous measurements of flow velocity and bed morphology are necessary. The latter causes significant problems under flowing water conditions, and different methods have been proposed over the past decades.

Until recently, it was common practice to measure bed form characteristics by using mechanical techniques like point gauges. Modern bed form measuring methods for use on a laboratory scale can be primarily divided in acoustic and optic techniques. Acoustic techniques (Abad & Garcia, 2009; Hurther et al., 2011; Muste et al., 2016; Naqshband et al., 2014; Thorne & Hanes, 2002) have the advantage that acoustic instruments can be used to measure both flow velocities and bed profiles and that they can be used up to large depths, even in the field (Gaeuman & Jacobson, 2007; Simpson & Oltmann, 1993). However, they need to be submerged, causing a disturbance of the experiment and increasing the minimal water depth needed in experiments. Optic techniques can be divided in digital photogrammetry (Aberle et al., 2009; Butler et al., 2002; Henning et al., 2009; Lane et al., 2001) and monochromatic lasers (Abad & Garcia, 2009; Friedrichs & Graf, 2006; Huang et al., 2010; Peña González et al., 2007; Visconti et al., 2012). Optic methods do not have the disadvantages mentioned above, but are limited to small water depths due to visibility of the reflected

signal, which is affected by attenuation, refraction and scattering. This, however, is not a major issue on a laboratory scale, as long as surface waves causing scattering and changes in refraction are limited.

Different laser-based techniques have been proposed in the past. Monochromatic laser stripes (Huang et al., 2010) or sheets (Abad & Garcia, 2009) captured by a camera are limited to small spatial scales or to a single transect, respectively. In the field, a hand-held laser scanner was used by Smart et al. (2004) to determine bed roughness. On a larger scale, airborne lasers for topographic mapping are long-known as Light Detection And Ranging (LiDAR) (Guenther, 1985; Krabill et al., 1984). Measurements with similar methods for laboratory experiments have been performed with point laser scanners for dry-bed (Yeh et al., 2009), still water (di Risio et al., 2010) and flowing water conditions (Visconti et al., 2012), providing bed level data in a nonintrusive way during the experiment. Line laser extensions of this method have been used by Peña González et al. (2007) (dry-bed and still water) and Friedrichs and Graf (2006) (flowing water). As opposed to LiDAR, laboratory laser scanners are also used to measure subaqueous topography, which comes at the cost of additional errors and a considerable amount of missing data.

Visconti et al. (2012) provide a thorough description of the use of a point laser scanner for measuring bed profiles in laboratory experiments. Their method consists of simultaneous continuous monitoring of the bed level (using a point laser facing vertically downward, coupled to a CCD) and the water level (using an ultrasonic level transmitter). Their study primarily aimed at overcoming the difficulties of the use of this new measurement approach, quantifying different sources of measurement errors and determining the accuracy of the method (after calibration and corrections), as it was applied successfully in a practical way both in studying tidal systems (Stefanon et al., 2010; Tesser et al., 2007) and fluvial systems (Visconti et al., 2010). A comparable method using a line laser was previously applied by Peña González et al. (2007). However, they only did experiments with still water and did not study the dependence of the measurement error on water depth in detail. Therefore, a thorough analysis of the measurement errors as done by Visconti et al. (2012) for line laser scanner applications would be valuable for application in future movable bed experiments.

In the present study, the full swath width of a line laser is taken into account in order to assess the possibilities of a line laser scanner for continuous monitoring of bed forms during a moving bed physical scale experiment, without disturbing the flow. To improve existing data processing approaches, the application of a robust LOcally weighted regrESSion (LOESS) algorithm is tested that accounts for outliers and missing values due to scattering at the water surface (Cleveland, 1979; Cleveland & Devlin, 1988). In the remainder of this paper, section 2 offers details of the measurement principles, the line laser set-up and the LOESS-based algorithm. In section 3, the measurements are presented and the effect of applying corrections is illustrated. Section 4 discusses problems and benefits of the use of this new measurement procedure. Finally, the experimental findings are concluded in section 5.

2. Measurement Principles

2.1. Set-up

Experiments were carried out at the Kraijenhoff van de Leur Laboratory for Water and Sediment Dynamics (Wageningen University and Research) in a flume of 0.5 m×1.2 m×14.4 m (height×width×length) with facilities for recirculation of both water and sediment. At the start of the flume, a stacked pile of PVC tubes acts as a laminator of the flow to suppress turbulence. The flume is equipped with an electromagnetic flow meter to monitor discharge, and eight tubes on the left side of the flume (looking downstream), coupled to stilling wells outside the flume. Each stilling well contains a magnetostrictive linear position sensor to monitor water levels. Looking downstream, the right side wall of the flume was roughened with the intention to create a transverse bed slope, which will be studied in a future project.

The here proposed bed-form measurement method consists of a line laser and a 3-D camera with Gigabit Ethernet (SICK, 2012), both mounted on a measurement carriage that can move on fixed rails along the flume. The beam swath angle of the line laser is 50.0°, covering a width of 419 mm of the bare flume bottom at an installation height of 449 mm. This width decreases evidently when a layer of sediment is present. The projected laser line is oriented perpendicular to the flow direction, and the camera is looking under an angle (see Figure 1). The bed profile is measured by means of triangulation. Because of the limited width of the laser beam swath, multiple parallel (partly overlapping) tracks are used to measure the whole width of

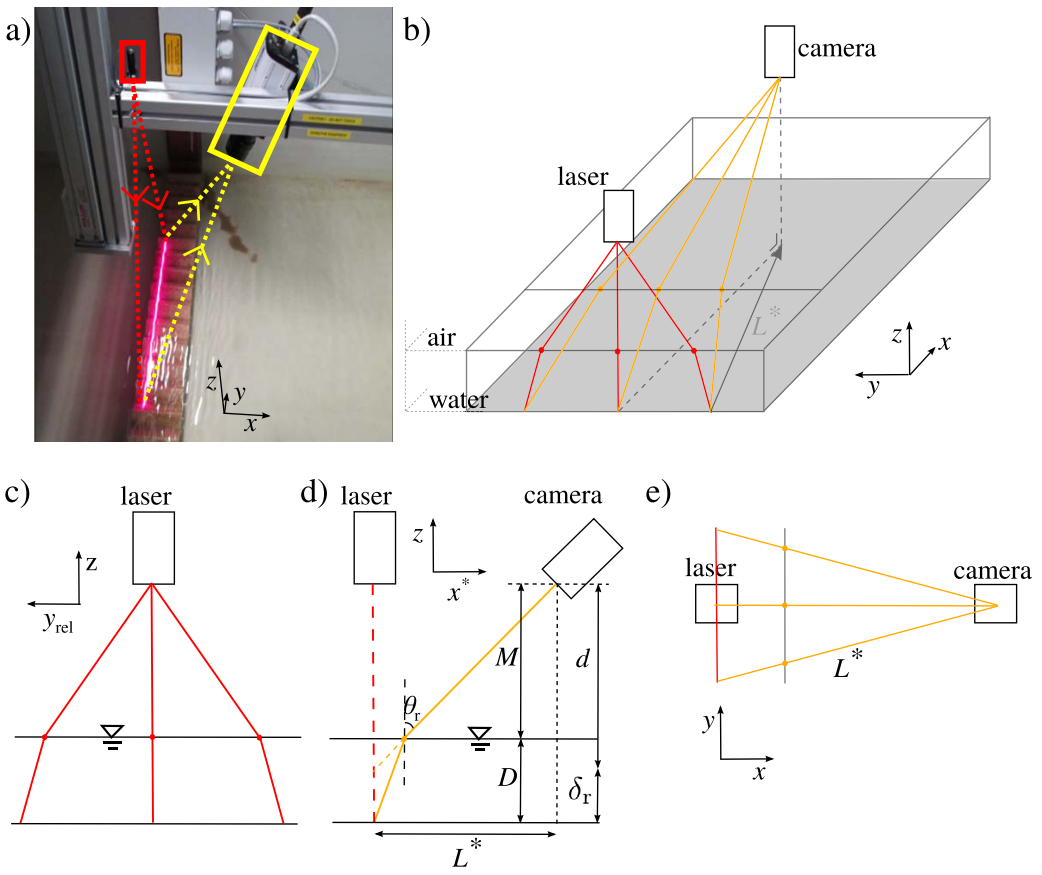

Figure 1. (a) Picture of the line laser scanner measuring a sawtooth profile. The red light on the profile is the line emitted by the laser. (b) Overview of the experimental set-up. Red lines indicate transmitted laser beams and yellow lines indicate reflected laser beams, measured by the camera. c) Front view of the flume showing the transmitted laser beams. d) Vertical cross section of the flume over L^*, with x^* the projection of x onto L^*, showing the reflected laser beams including the measures used in equation (4). e) Top view of the flume.

the flume, with along-track resolution Δx. These tracks are schematized in Figure 2, where the left two sketches indicate configurations used in experiments without sediment, and the right two sketches indicate the configuration used in experiments with sediment. Additionally, the overlap between the tracks is indicated. In the rightmost configuration, it takes less than five minutes (4′24″) to cover the whole flume in this study.

Five consecutive series of experiments were performed, viz. measurement of the bottom profile of 1) an empty flume, 2) a flume with still water only, 3) a flume with flowing water, 4) a flume with a movable bed consisting of sand with a density of $\rho_s = 2650\,\mathrm{kg/m^3}$ and a size of $D_{50} = 0.719\,\mathrm{mm}$ and $D_{95} = 0.962\,\mathrm{mm}$, and 5) a flume with a movable bed consisting of polystyrene granules with a density of $\rho_s = 1055\,\mathrm{kg/m^3}$ and a size of $D_{50} = 2.1\,\mathrm{mm}$ and $D_{95} = 2.9\,\mathrm{mm}$. An overview of the different runs during these experiments is given in Table 1. As can be seen, in what is called the still water case, discharge was kept at a minimum value of $3\,\mathrm{L/s}$, determined by the technical construction of the flume causing downstream leakage. In moving bed experiments, the bed profile changes during the measurements. This is dealt with by analysing one track at a time, and correcting for an average dune celerity when comparing the results to consecutive dry bed results.

2.2. Calibration and Corrections

Due to properties of the camera lens, deformations in the obtained image occur. Also, perspective distortion occurs, dependent on the distance of the bed from the camera and the angle under which the camera

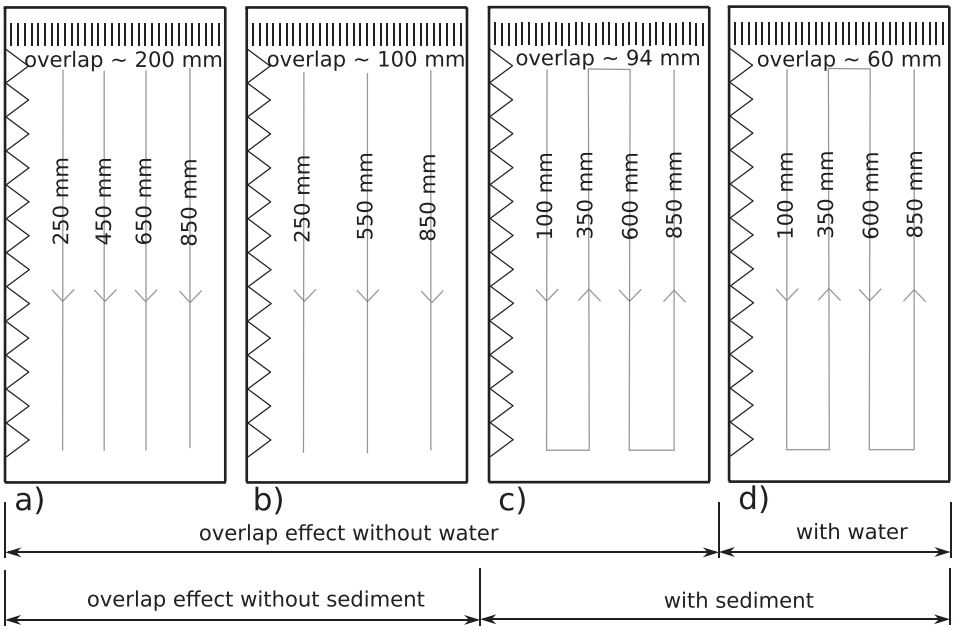

Figure 2. Tracks of the line laser scanner for the different experiments (with *y*-coordinate of the laser indicated), including the overlap between the laser swaths of different tracks. Configurations in Figures 2a and 2b are used during experiments without sediment, whereas Figures 2c and 2d indicate experiments with sediment without and with water, respectively. Triangles indicate the roughened side wall and lines at the top indicate the laminator (see section 2.1).

is looking (SICK, 2012). Both deformations are taken care of by an internal calibration of the 3-D camera, converting the internal camera coordinates to real-world coordinates. However, two additional corrections are needed: a background correction (δ_b) and a refraction correction (δ_r), as described below.

The former of these corrections accounts for structural deviations in the measured bed profile, as measured with high accuracy using both a ruler and data points vertically under the laser device. To determine the background correction, three consecutive steps were taken: 1) determining a best fit of the flume bottom, 2) determining how much the measured bed level of the laser scanner is off, 3) fitting this error to be used in measurements in which the bed level is a priori unknown.

Table 1
Overview of the Runs Performed During the Five Experiments[a]

#	Δx (mm)	Water	Q (L/s)	Sed.	u (m/s)	Fr	Runs	Laser path
1	1	×		×			10	a
2	1	✓	3	×			10	a
3	1	✓	8	×	0.10	0.11	1	a
	5	✓	20	×	0.08–0.29	0.10–0.25	3	b
	1	✓	30	×	0.12–0.28	0.08–0.29	6	a
	1	✓	40	×	0.17–0.47	0.12–0.54	6	b
	1	✓	60	×	0.20–0.44	0.12–0.40	5	a
4	2	✓	70	✓	0.55	0.54	1	c/d
	2	×		✓			1	c/d
5	2	✓	20	✓	0.16	0.16	1	c/d

[a]The columns consecutively show the experiment number, along-track resolution, presence of water, discharge, presence of sediment, (range of) mean flow velocity, (range of) Froude number, number of runs, and the laser path (i.e., the path of the laser scanner as illustrated in Figure 2). The runs within experiments 2 and 3 differ in water level (see Figures 5 and 6, respectively). For the runs with flowing water in experiments 4 (sand) and 5 (polystyrene), the mean water levels are 11 cm and 10 cm, respectively.

The first step is achieved by fitting a second order polynomial through the data points vertically under the laser (cf. y_{laser} in Figure 1c) for a range of x-values. This results in a best fit of the high-accuracy bare flume bottom

$$\hat{z}(x,y)=\hat{z}(y)=a_1y^2+a_2y+a_3, \tag{1}$$

Second, a structural deviation of the measured height from the high-accuracy flume bottom is defined as

$$\epsilon_{st}(x,y)=z(x,y)-\hat{z}(x,y), \tag{2}$$

with z the measured bare flume bottom.

As a third and final step, this structural deviation ϵ_{st} is plotted against the relative transverse position y_{rel}, for each track in an empty flume. y_{rel} is a transverse coordinate that is fixed with respect to the measurement carriage (origin at the right boundary of the camera window), whereas y and y_{laser} (i.e., the transverse position of the laser in the flume) are fixed with respect to the flume (origin at the right wall of the flume). The background correction is then obtained from fitting a second order polynomial as

$$\delta_b(y_{rel})=b_1y_{rel}^2+b_2y_{rel}+b_3, \tag{3}$$

which is subtracted from the measured vertical position z. A visualization of this approach can be found in Figure 4, showing results for different x-values, averaged over 10 measurements.

The purpose of the present study is to be able to track submerged bed forms during the experiment, which requires a second correction (δ_r) taking care of the refractions at the air-water interface. These refractions cause a deviation in the transverse measuring location and in the measured bed level, see Figures 1c and 1d.

Based on the geometry shown in Figure 1, a formula for the refraction correction is formulated as

$$\delta_r=\left[1-\frac{M}{d}\right]\left[\frac{L^*}{\tan\left[\arcsin\left(\sin\theta_r/n\right)\right]}-d\right], \tag{4}$$

where M is the distance between the camera focal point and the water level, d is the distance between the camera focal point and the apparent bed level height (Figure 1d), n is the ratio of refraction indices of water and air, L^* is the projection of the laser path on the bottom of the flume (Figure 1e), and the angle of refraction $\theta_r=\arctan\left(L^*/d\right)$. The correction δ_r is also subtracted from the measured vertical position z of the bed to receive the estimated level of the bed $z_a=z-\delta_b-\delta_r$.

2.3. Statistical Analysis

A statistical analysis of the experimental results is performed, focussing on the results of the flowing water experiment in particular. For each run, the residual error is calculated using

$$\epsilon(x,y)=z(x,y)-z_{dry}(x,y), \tag{5}$$

with z_{dry} the dry-bed level. The mean ($\bar{\epsilon}$) and standard deviation (σ_ϵ) of the residual error are calculated over all data points, as defined by

$$\overline{X}=\frac{1}{N}\sum_{i=1}^{N}X_i$$

$$\sigma_X=\sqrt{\frac{1}{N-1}\sum_{i=1}^{N}\left(X_i-\overline{X}\right)^2}, \tag{6}$$

with N the number of data points per run. From these, the coefficient of variation is defined as $\sigma_\epsilon/|\bar{\epsilon}|$. The variables $\bar{\epsilon}$, σ_ϵ and $\sigma_\epsilon/|\bar{\epsilon}|$ give an indication of the average overestimation of the bed level and its absolute and relative variation during one experiment, respectively. Moreover, correlations between variables are defined using the Pearson moment-product correlation coefficient, which for variables A and B is defined as

$$\varrho=\frac{1}{N}\sum_i\left(\frac{A_i-\overline{A}}{\sigma_A}\right)\left(\frac{B_i-\overline{B}}{\sigma_B}\right). \tag{7}$$

This coefficient is used to study the influence of flow velocity, water depth and laser beam angle on the spread and the missing of data points in the measurement of the bed profile. Lastly, to define a measure for the measurement error during a specific experiment, a root-mean-square error is calculated between bed level values with and without water as

$$\mathrm{RMSE} = \sqrt{\overline{\epsilon^2}} = \sqrt{\overline{(z - z_{\mathrm{dry}})^2}}. \tag{8}$$

The root-mean-square error is a function of the submerged and dry-bed mean bed levels, the submerged and dry-bed standard deviations and the Pearson moment-product correlation coefficient (Gupta et al., 2009; Murphy, 1988) as

$$(\mathrm{RMSE})^2 = (\overline{z_1} - \overline{z_2})^2 + \sigma_1^2 + \sigma_2^2 - 2\sigma_1\sigma_2\varrho_{1,2}, \tag{9}$$

where subscripts 1 and 2 indicate the submerged and dry-bed measurements, respectively.

2.4. Data Interpolation and Outlier Removal

Outliers and missing data have to be corrected for in moving bed experiments by applying a smoothing and interpolation algorithm. Because of the irregularly spaced nature of the retrieved data, an algorithm that does not need interpolation to a regular grid beforehand is prefered. A LOcally weighted regrESSion algorithm (LOESS) (Cleveland, 1979; Cleveland & Devlin, 1988) is an appropriate choice (e.g., Plant et al., 2002; Vermeulen et al., 2014). This interpolation and smoothing method is based on a polynomial fit to the data using weighted least squares. For each fitted value at (x_k, y_k) a fixed number of nearest neighbours is taken into account (defined by a smoothing fraction f of the total number of data points), with the weight decreasing with increasing distance from (x_k, y_k). This makes it a clearly two-dimensional method. The computational effort to apply a LOESS procedure can become too high for a large domain. Therefore, the procedure is split in two consecutive steps. An initial data reduction operation is applied by projecting the scatter data onto a regular grid, based on linear LOESS interpolation (Cleveland, 1979). A tricube weight function is used for this, choosing 50 nearest neighbours, and a grid with 10 mm spacing. Then, the same LOESS procedure is repeated using gridded data, which is now feasible with a larger fraction of the gridded data set. We choose $f = .002$, corresponding to 235 nearest neighbours. In both steps, the solution is obtained iteratively; two and five iterations were needed to achieve convergence in both steps, respectively.

In the remainder of this article, the terminology 'not applying a LOESS fit' is used when only the first step is applied—which is almost equivalent to interpolation of the data to a regular grid—unless explicitly stated otherwise. The above parameter values are determined by applying different sets of parameter values and optimizing the Pearson moment-product correlation coefficient (equation (7)) between measured bed profiles in the dry-bed and in the flowing water cases. Also, the processed bed profile was inspected visually. The resulting bed profile was insensitive to small changes in LOESS parameter values. The nearest neighbours are determined including an elongation parameter which aligns with the main dune dimension to make sure that the dune crest is not smoothed out significantly. This parameter, which value is again determined following the above approach, makes the span of the LOESS fit elliptical instead of circular. The eccentricity of the elliptical span is $\varepsilon = .87$ and $\varepsilon = .94$ in steps (1) and (2), respectively, with the semi major axis in the cross-flow direction.

2.5. Validation

Where direct validation of the measured bed profile is possible in the case of measuring the flume bottom or a fixed profile, this is cumbersome in moving bed experiments. In such experiments, the dry-bed profile at the time of measurement is unknown. However, the final bed profile can be measured accurately under dry-bed conditions after the experiment. Only the last complete scan of the flume under flowing water conditions is therefore analyzed. To a limited extent, the bed forms continue to migrate after the last laser scan, because the flow in a flume cannot be stopped instantly. The validation profile (i.e., the dry-bed profile) is adjusted to the situation during the last swipe by shifting the bed morphology map using an estimated bed form celerity, as determined by

$$x_i' = x_i - c_b(t_N - t_i), \tag{10}$$

with x_i the location of a dry-bed data point and x_i' the manipulated location. The property $c_b = \Delta x_{\mathrm{crest}}/\Delta t$ is an estimation of the bed form celerity, determined from the shift of dune crests between flowing water and

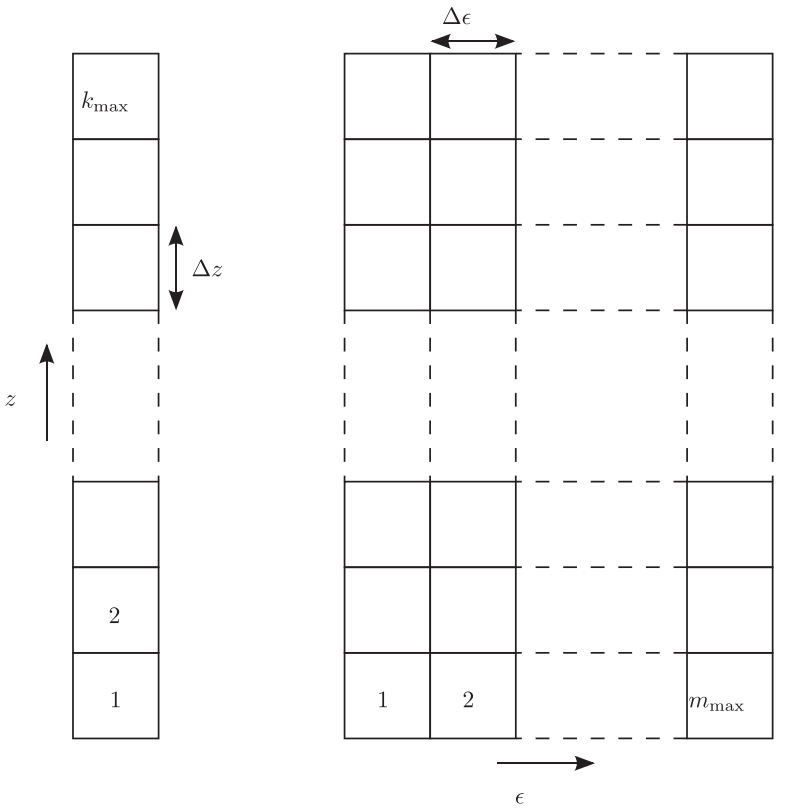

Figure 3. Schematic illustration of the mapping of bed profile measurements in bins. Left: only bed level bins (of size Δz). Right: both bed level bins (vertical) and residual error bins (horizontal, of size $\Delta\epsilon$).

dry-bed measurements (Δt being the time interval between start of the last measured swipe with flowing water and the end of the flowing water experiment), and t_i is the measurement time of the i^{th} data point ($i=1,\ldots,N$ with N the total number of data points covering the flume).

In addition to the above validation, the applicability of the LOESS fitting algorithm on bed level datasets with both data gaps (i.e., missing values) and measurement errors (i.e., data scattering around the dry-bed profile) is studied. The applied method in this study for both cases is described below.

The spatial structure of data gaps (as a function of bed level) is determined by defining $k_{\max}$ regularly spaced bed level bins of width Δz. The bed level bins are schematically visualized in the left part of Figure 3. Now the probability p_k of a bed level value to be missed by the measurement device is defined by the number of dry-bed data points in the k^{th} bed level bin for which the corresponding submerged bed level value is not measured, divided by the total number of dry-bed level values in the k^{th} bed level bin, all along the last-measured track. The correction for bed form celerity of equation (10) is applied. From the probability mass function p_k and the dry-bed profile, N_s bootstrap samples are created, by generating a random number α from a standard uniform distribution for each of the data points in the dry-bed profile. If $\alpha < p_k$ for the bed level bin corresponding to this data point, the measured value is removed. The LOESS algorithm is applied to all bootstrap samples consecutively. Finally, mean and standard deviation were determined, together with Pearson moment-product correlation coefficient and root-mean-square error compared to the dry-bed profile (cf. equations (6–8)) and values before and after LOESS fitting are compared.

To determine the spatial structure of the residual error ϵ, a similar procedure is followed. Yet additionally $m_{\max}$ residual error bins of width $\Delta\epsilon$ are introduced (see right part of Figure 3). Probability p_k is replaced by the probability $p_{k,m}$ that a bed level value in the k^{th} bed level bin is measured with a residual error in the m^{th} residual error bin. Now $p_{k,m}$ is defined by the number of dry-bed data points in the k^{th} bed level bin for which the corresponding submerged bed level value has a residual error within the m^{th} residual error bin,

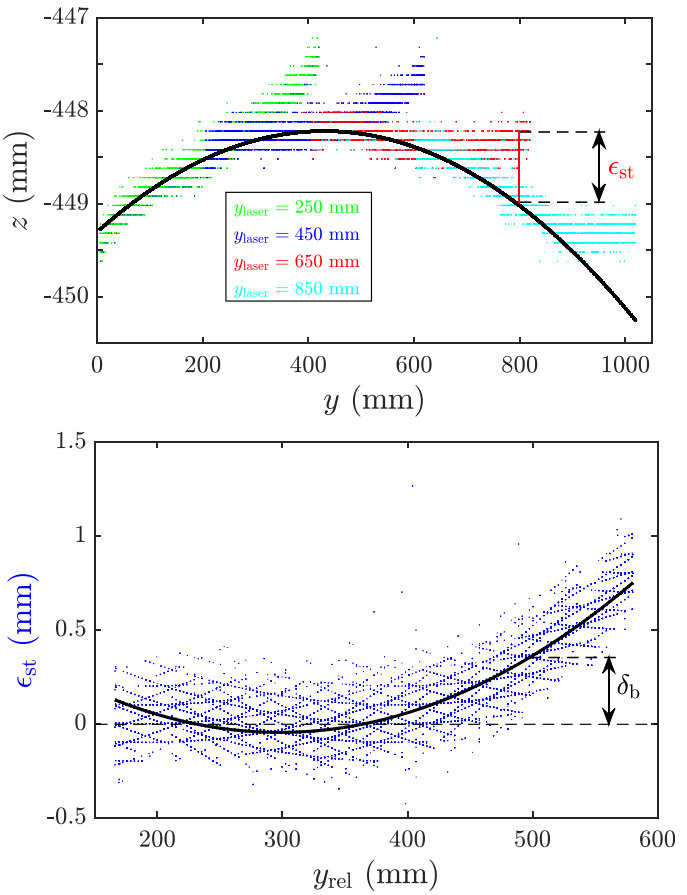

Figure 4. (top) Height of the empty flume bottom for experiments 1 to 4, measured in four tracks. The solid black line indicates a fit through the data points vertically under the laser, representing the high-resolution flume bottom. (bottom) The residual error ϵ and the background correction δ_b, shown as a solid black line, cf. equations (2) and (3).

divided by the total number of dry-bed data points in the k^{th} bed level bin, all along the last-measured track. The mathematical definitions of the bed level and residual error bins can be found in Appendix A.

3. Results

3.1. Fixed Bed Experiments

3.1.1. No Water

The results for measurements of the bare flume bottom are visualized in Figure 4, where the colours indicate the four different tracks (each averaged over ten measurements). The fit representing the high-resolution flume bottom is indicated by the solid line. Each track shows a deviation on the right-hand side, which residual error is corrected for by fitting equation (3) (using a vertical setting of $M+D=449$ mm at $x=1000$ mm and $y=500$ mm). The obtained correction parameters a_i and b_i can be found in Appendix B.

3.1.2. Still Water

When water is present in the flume, laser refraction affects the results. Therefore, the correction of equation (4) is applied to ten different water levels (lower graph of Figure 5) after applying the background correction. Discharge is kept at a minimum value of 3 L/s, determined by the technical construction of the flume causing downstream leakage. Because of the refraction of laser light at the air-water interface, the distance between laser and flume bottom is increasingly underestimated with water depth. Moreover, deviations increase toward the side of a track because of an increasing travelling path of the laser light through water.

Mean and standard deviation of the residual error ϵ, that remain after corrections, are shown in the upper graph of Figure 5. The percentage of missing values per run are plotted in the lower graph of Figure 5, showing an increase of missing values with water depth.

3.1.3. Flowing Water

For measurement of the bare bottom with flowing water, the background and refraction corrections are consecutively applied as explained above. The hydrodynamic conditions parametrized by water depth (D), flow velocity (u), Froude number ($Fr=u(gD)^{-1/2}$) and Reynolds number ($Re=uDv^{-1}$), with v the kinematic viscosity) are shown in the lower graph of Figure 6. The resulting mean and standard deviation of the residual error and the percentage of missing values are shown in the upper two graphs of Figure 6, respectively.

3.1.4. Correlations

In the left four columns of Figure 7, the correlation of the absolute mean residual error $|\overline{\epsilon}|$, standard deviation σ_ϵ, coefficient of variation $\sigma_\epsilon/|\overline{\epsilon}|$ and the percentage of missing values with the water depth D, flow velocity u, Froude number Fr and Reynolds number Re are shown for the flowing water experiment. These correlations reveal that the absolute mean measurement error $|\overline{\epsilon}|$ increases with velocity. Values of σ_ϵ with Reynolds number, or specifically both with water depth and with velocity. The relative spread of the residual error, $\sigma_\epsilon/|\overline{\epsilon}|$, and the percentage of missing values increase with depth. In calculating the correlations, run 19 is omitted, due to 97.1% missing values. During this run with large data losses, the sediment pump may have been clogged with sediment. If such a situation occurs, and the plug of sediment releases, a situation may occur that results in a large number of missing values because of a high suspended sediment concentration. Runs 16 and 21 are omitted in the correlations with $|\overline{\epsilon}|$, σ_ϵ and $|\overline{\epsilon}|/\sigma_\epsilon$, because of the disproportionally large values of σ_ϵ.

The rightmost column of Figure 7 shows the correlation of the absolute mean residual error $|\overline{\epsilon}|$, the standard deviation σ_ϵ, the coefficient of variation $\sigma_\epsilon/|\overline{\epsilon}|$ and the percentage of missing values with the absolute deviation from the mean relative transverse distance $|y_{rel}-\overline{y_{rel}}|$. The latter is a measure for the laser beam angle. It is shown that especially the spread in residual error and the percentage of missing values increase

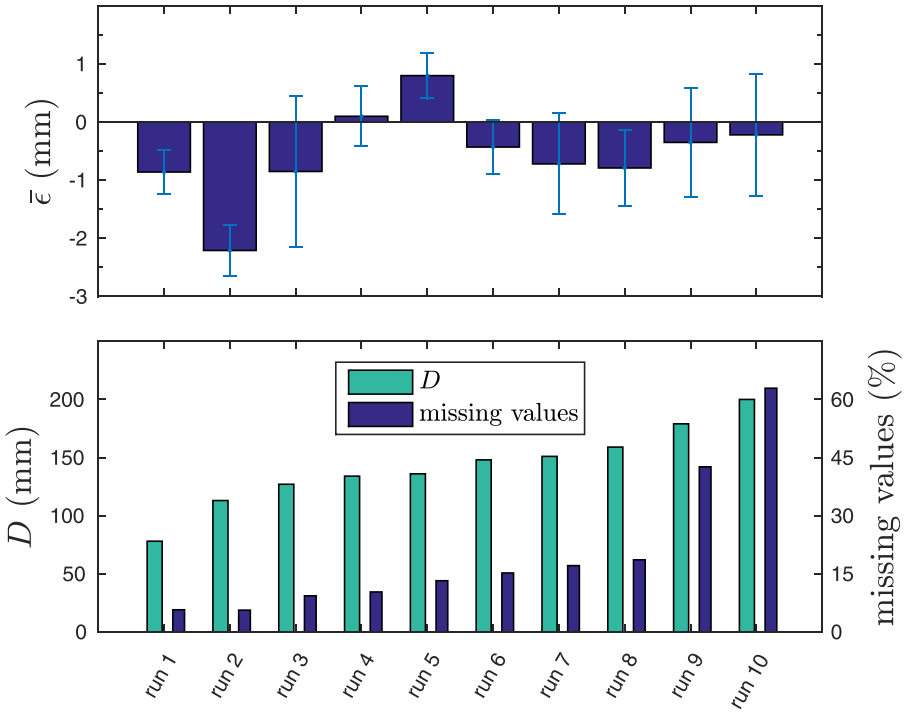

Figure 5. Conditions during the 10 runs performed under still water conditions. (top) Mean and standard deviation of the residual error. (bottom) Water depth D and percentage of missing values.

with beam angle. The 5% largest values of the coefficient of variation are considered outliers, and are therefore omitted in calculating the correlation.

3.2. Movable Bed

3.2.1. Performance of the LOESS Procedure

Compared to the fixed bottom experiments discussed above, bed movement causes a large percentage of missing values (71% on average over the whole flume in the sand bed case of the present study). Redundancy in the data still allows to retrieve a workable and reliable bed profile, after application of the LOESS algorithm.

An overview of the studied variables for the moving bed experiments is given in Table 2, viz. the mean and standard deviation of the bed level, the Pearson moment-product correlation coefficient for the dry-bed profile and the root-mean-square error, also based on the dry-bed profile. These are obtained for ensembles of the original bootstrap samples, samples after the first step of LOESS based gridding and samples after the second step of the LOESS procedure. Each ensemble consists of $N = 50$ samples. As an example, for each of the three situations depicted in Table 2 a cross section at $y = 921$ mm of one of the used profiles is shown in Figure 8, illustrating the dry bed profile, the bootstrap sample, the one-step LOESS procedure and the two-step LOESS procedure of the bootstrap sample.

From Table 2 and Figure 8 it can be concluded that the root-mean-square error after application of the LOESS procedure is significantly smaller than 1 cm, whereas the dunes are typically of order 3−4 cm. Missing values mainly contribute to a slight increase of the mean bed level (which is compensated for by the LOESS procedure) and a decrease in standard deviation of the profile (which is partly compensated for by the LOESS procedure). Scattering of measured values mainly contributes to a slight lowering of the mean bed level, a slight increase in the standard deviation of the profile (which is largely overcompensated for by the LOESS procedure) and a decrease in the correlation coefficient, which is compensated for by the LOESS procedure. Overall, the LOESS algorithm increases the correlation coefficient and reduces the root-mean-square error at the cost of both a lower standard deviation (i.e., flattening of bed forms) and a slightly lower mean bed level of the profile (caused by data scattering).

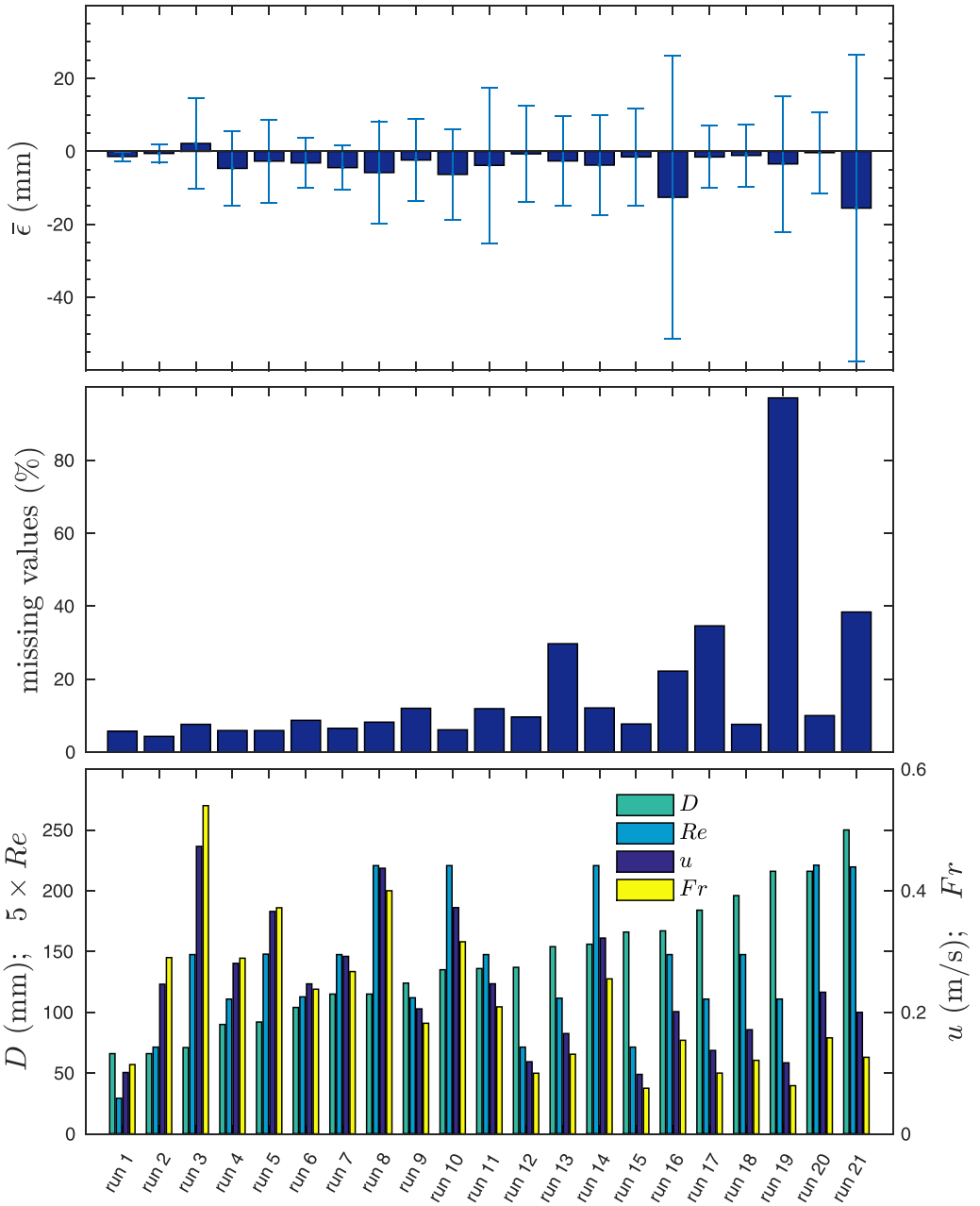

Figure 6. Conditions during the 21 runs performed under flowing water conditions. (top) Mean and standard deviation of the residual error. (middle) Percentage of missing values. (bottom) Water depth, flow velocity, Froude number and Reynolds number.

3.2.2. Sand With Flowing Water

Despite the large percentage of missing values, the bed profile can still be retrieved with reasonable accuracy when a LOESS procedure is applied. This is illustrated in Figure 9a, showing the LOESS fitted values of the bed as measured under flowing water conditions at $y = 881$ mm (upper graph, dashed curve). Moreover, the dry-bed profile (retrieved after emptying the flume and correcting for a mean bed form celerity of $c_b = 2.9$ mm/s) is shown both with and without applying the LOESS algorithm (upper graph, light and dark solid curve, respectively). Despite the large number of missing values (over 50% on the transect used in Figure 9a), the Pearson product-moment correlation coefficient between the LOESS fitted values under flowing water conditions and the dry-bed profile is relatively high: $\varrho = .798$ and $\varrho = .755$ for the dry-bed profile with and without applying the LOESS algorithm, respectively.

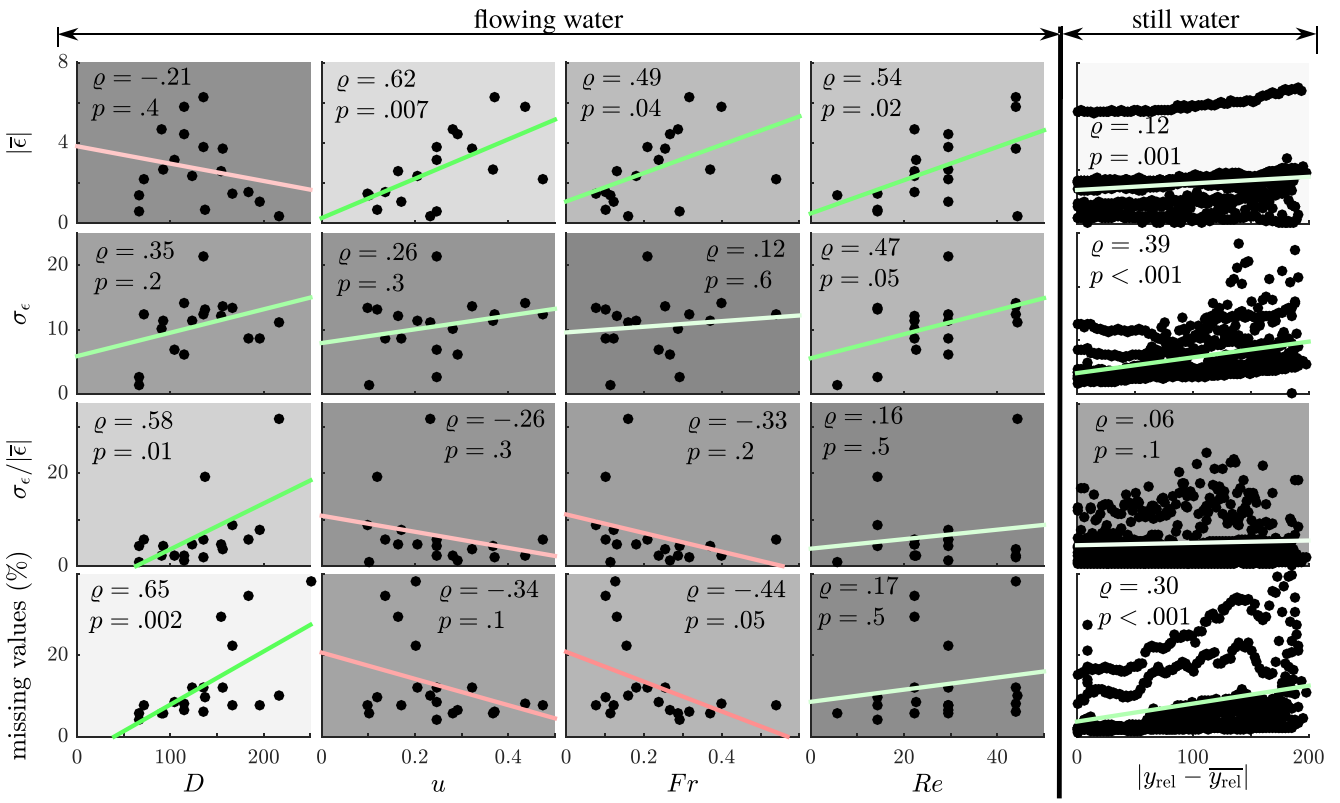

Figure 7. First 4 columns: Flowing water correlations between absolute mean residual error ($|\overline{\epsilon}|$), standard deviation of the residual error (σ_ϵ), coefficient of variation ($\sigma_\epsilon/|\overline{\epsilon}|$) and percentage of missing values, and water depth (D), flow velocity (u), Froude number (Fr) and Reynolds number (Re). Both the Pearson product-moment correlation coefficient ϱ and the p-value are given. The latter is also reflected by the grey-scale of the background and the former by colour and intensity of the regression line. Run 19 is excluded, due to the high percentage of missing values related to a polluted pump. Runs 16 and 21 are omitted in the correlations with $|\overline{\epsilon}|$, σ_ϵ and $\sigma_\epsilon/|\overline{\epsilon}|$. Rightmost column: Still water correlations between $|\overline{\epsilon}|$, σ_ϵ, $\sigma_\epsilon/|\overline{\epsilon}|$ and percentage of missing values, and absolute deviation from the mean relative transverse distance $|y_{rel} - \overline{y_{rel}}|$ (representing the laser beam angle). The 5% largest values are omitted in the correlation of $\sigma_\epsilon/|\overline{\epsilon}|$ and $|y_{rel}|$.

The lower graph of Figure 9a shows the difference between the LOESS fitted bed profile under flowing water conditions and the dry-bed profile with (light curve) and without (dark curve) application of the LOESS algorithm. Vertical dashed lines indicate levels of $\sigma_z/2$ and σ_z of the unfitted bed profile without

Table 2
The Effect of LOESS Fitting on a Bed Level Data Set With Missing Data and/or Scattered Data on Bed Level Statistics[a]

LOESS		$\overline{z}$ (mm)	σ_z (mm)	ϱ	RMSE (mm)
Dry	no	−359.99	18.18	—	—
Gaps	no	−357.44	14.62	1.00	0.00
	1st	−359.79	17.23	.97	4.33
	2nd	−359.77	16.26	.95	5.78
Scatter	no	−362.78	19.43	.78	12.85
	1st	−361.98	14.73	.93	7.32
	2nd	−361.67	13.39	.94	7.43
Both	no	−360.35	17.19	.78	11.47
	1st	−361.74	14.46	.93	7.32
	2nd	−361.49	13.31	.94	7.47

[a]Consecutive columns indicate mean bed level, standard deviation of the bed level, correlation coefficient between the fitted profile and the dry-bed profile, and root-mean-square error between the fitted profile and the dry-bed profile. For each case an ensemble of 50 bootstrap bed profiles is taken into account. For comparison the raw bootstrap ensembles (without applying the LOESS fitting algorithm) are also shown.

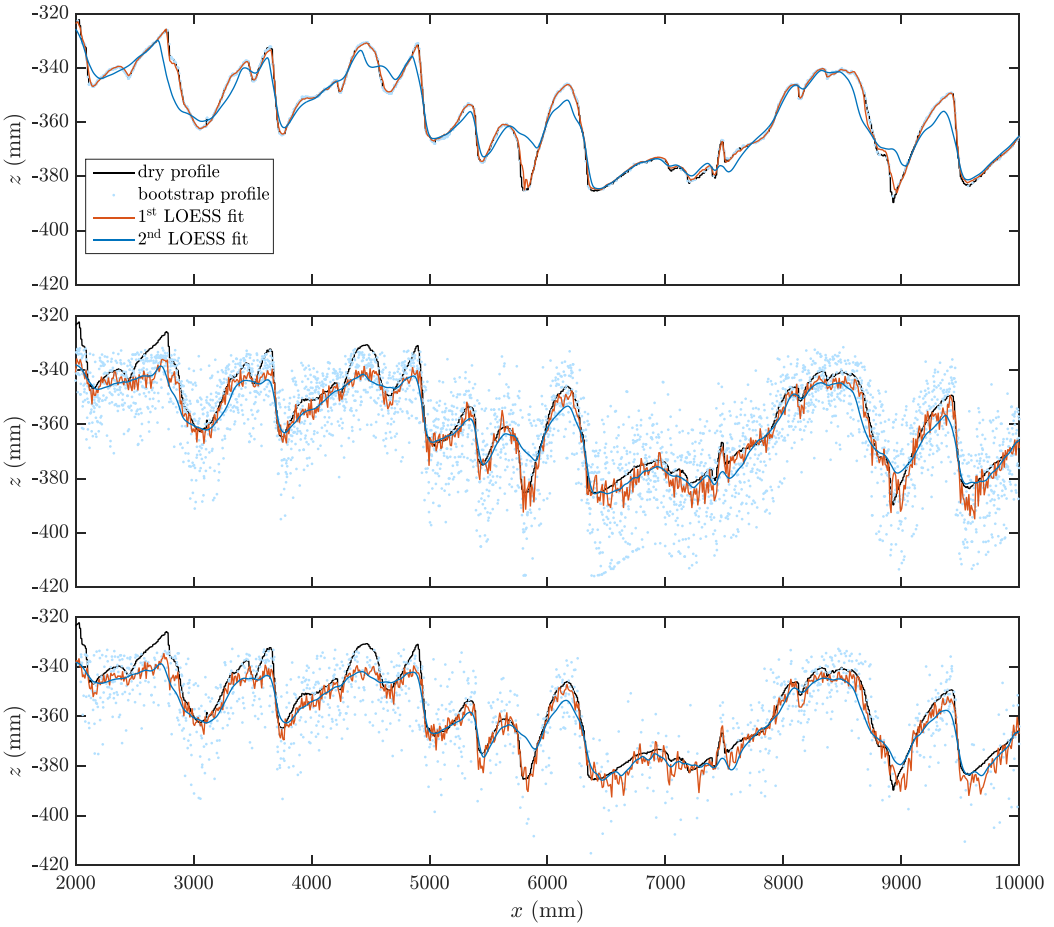

Figure 8. Example at $y=921$ mm of one of the profiles from a 50-profile bootstrap ensemble. From top to bottom, bootstrap samples for the effect of (a) missing data, (b) scattered data and (c) both are shown.

water. On average, bed profiles are slightly underestimated under flowing water conditions, but stay largely within σ_z from both the LOESS fitted and the unfitted dry-bed profile.

To emphasize the deviations of the LOESS fitted flowing water values from the dry-bed profile, the measured bed levels with flowing water are plotted against those without water in the right graph of Figure 9a, both with (light dots) and without (dark dots) applying the LOESS algorithm. It is clear that deviations are larger for lower bed levels (in other words: for increasing water depth). In addition to the Pearson product-moment correlation coefficient, the root-mean-square error is shown, as defined in equation (8). It is slightly smaller for deviations from the LOESS-fitted than for those from the nonfitted dry-bed profile.

The fact that correlation coefficients are significantly lower and root-mean-square errors are significantly higher than in the bootstrap example of the previous subsection, is mainly a validation problem and not a deficiency of the measurement method, nor of the LOESS algorithm. The main cause for these differences can be attributed to time aliasing, which occurs due to the time it takes to cover the entire flume, averaging multiple snapshots into one static dune field.

3.2.3. Sand With Still Water

During emptying of the flume after the flowing water experiment, the profile was measured under still water conditions. Following the same approach as described above, the results are shown in Figure 9b. It is clear that the LOESS fitted measurements with and without water coincide excellently, because of little missing values and limited scatter at the water surface. Without application of a LOESS fit to the dry bed data, the residual error still falls mostly within a $\sigma_z/2$ band.

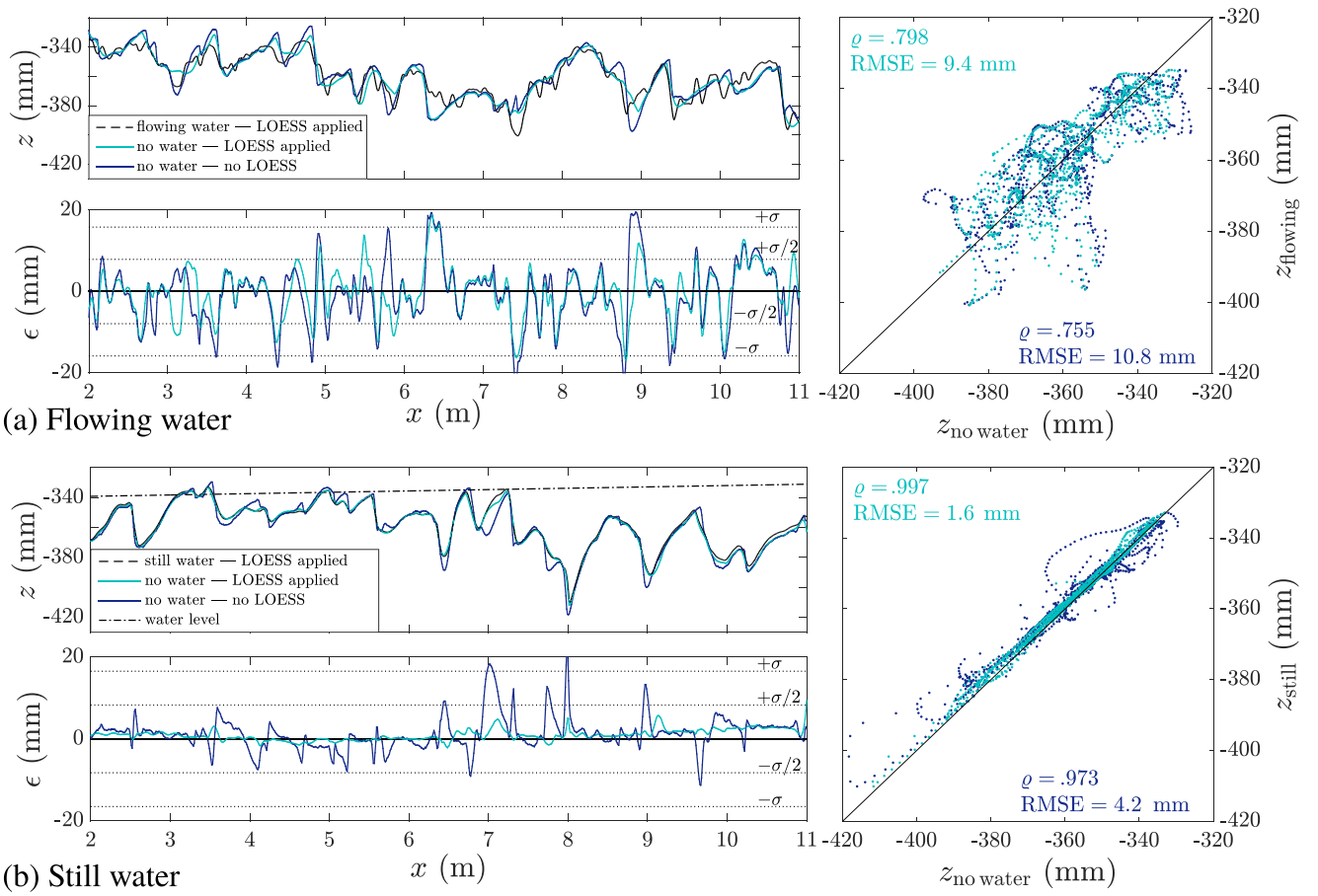

Figure 9. (a) End of the flowing water situation of experiment 4. (top) Slice of the bed profile at $y = 881$ mm, together with the dry-bed profile, corrected for bed form migration during and after the last laser scan, both with and without application of the LOESS algorithm. (bottom) The residual error of the bed profile measurements, both with (dashed curve) and without (dotted curve) application of the LOESS algorithm to the dry-bed data. σ indicates the standard deviation of the raw bed level data on the given transect. (right) Representation of the top figure in the (z, z)-plane. (b) Still water situation of experiment 4 (emptying of the flume). Top: Slice of the bed profile at $y = 326$ mm, together with the dry-bed profile (both with and without LOESS applied). The water level is indicated by a black dashed line. Bottom: The residual error of the bed profile measurements, both with (dashed curve) and without (dotted curve) application of the LOESS algorithm to the dry-bed data. Right: Representation of the top figure in the (z, z)-plane.

The right graph of Figure 9b shows small deviations from the bed-profile under still water conditions from the dry bed profile. For both situations, root-mean-square errors are small compared to the main bed form sizes, with a significantly larger RMSE for deviations from the nonfitted dry bed profile.

3.2.4. Comparing Sand and Polystyrene

As a check of the results obtained in section 3.1, i.e., $|\overline{\epsilon}| \propto u$ and percentage of missing values $\propto D$, a sand bed experiment is compared to a polystyrene measurement of the bed profile. Using polystyrene, small flow velocities and water depths suffice to create dunes that are dynamically similar to those in prototype rivers (Vermeulen et al., 2014). As shown in Figure 10, the sand case (top) shows much more scatter and more missing data compared to the polystyrene case (bottom).

4. Discussion

As shown in the previous section, the laser scanner detects the bottom of the flume accurately even under flowing water conditions, although the number of missing values clearly increases with increasing water depth. For larger depths, redundancy in the data can be exploited to estimate the complete bed topography. Hereafter, the key aspects in the approach are discussed.

Strictly speaking, the correction parameters b_i, which depend on the distance between the laser and the target measurement, should be determined after each calibration of the camera. The maximum background

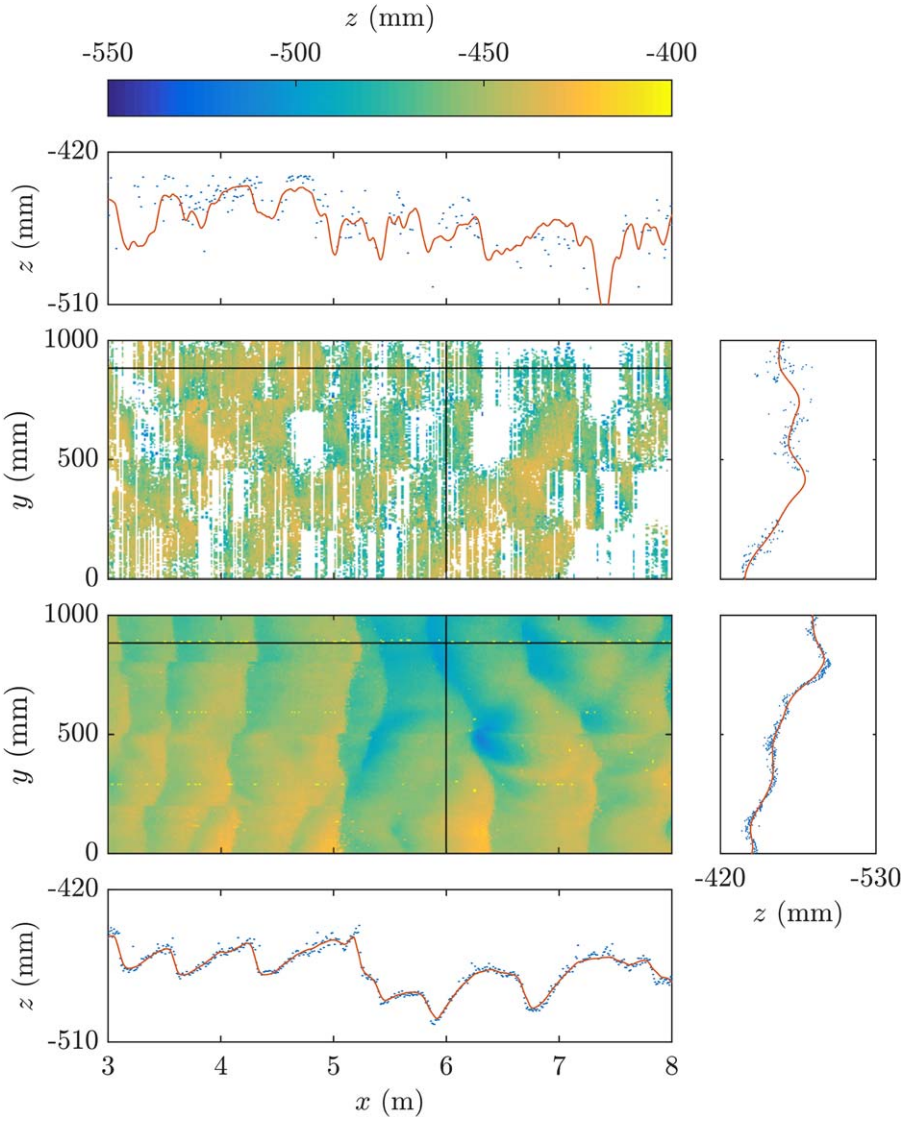

Figure 10. Colour plot (showing unfiltered measured bed level) and longitudinal and transverse bed profile along the black lines. For the profile data, blue dots indicate raw measurements, whereas red curves show the LOESS fitted results. The top half shows the results for experiment 4 (sand) and the bottom half for experiment 5 (polystyrene).

correction max (δ_b) is about 1 mm. This is roughly an order of magnitude smaller than the residual error for measurement of bed forms in a flowing water experiment (see Figure 9). Therefore, one may argue that for moving bed experiments, there is no need to apply a background correction and solely a refraction correction should suffice. In experiments with polystyrene, as described in section 3.2.4, deviations as large as shown in Figure 4 have not been observed.

In a previous study on measuring bed forms with a vertical point laser scanner, Visconti et al. (2012) found that the residual error increases with increasing water depth. This is confirmed in the present study both for the mean residual error $\bar{\epsilon}$ and for its standard deviation. These correlations need to be handled with care, as the number of data points ($N = 20$) is rather limited. It is expected that this is also highly dependent on turbidity—or concentration of suspended sediment—in the water column, as also suggested by Vargas-Luna et al. (2016). Turbidity, in turn, increases with increasing flow velocity.

As surface waves in a laboratory flume roughly increase in amplitude and wave number with increasing Froude number (Freeze et al., 2003), a larger measurement error is expected at higher Froude numbers. In

the present study the opposite is found, as the percentage of missing values decreases with increasing Froude number. Yet Freeze et al. (2003) evaluated much larger differences in Froude number, which mainly applied to measurements in the supercritical regime. At the upstream end of the flume (left in Figure 8), a structural underestimation of the bed level can be observed at the dune crests. This may relate to a higher water surface roughness in this region compared to downstream locations, leading to more scattering of the laser light.

Despite the expected difficulties when measuring a movable bed under flowing water conditions due to scattering by sediment particles, increased water surface roughness and spatiotemporal variability of the water depth, the bed is measured with reasonable accuracy. This is a promising first result toward future applications of dune tracking using a line laser scanner. This is especially the case for measurements under still water conditions (Figure 9b), as these largely reduce the water surface roughness and remove temporal variability of the water depth. When lightweight artificial sediments are used such as polystyrene as successfully used by (e.g., Hentschel, 2007; Vermeulen et al., 2014), dunes start to develop under smaller discharge and water levels, minimizing the error in the laser measurements. This is indeed confirmed by visually comparing the results of a sand experiment and a polystyrene experiment, with the latter under smaller flow velocities and water depths (Figure 10). To give an indication of the measurement error using the procedure described before, the RMSE should be determined in each new experimental setting, similar to the right graphs of Figure 9.

Time aliasing occurs as it takes time for the scanning device to cover the entire flume. For the example presented in section 3.2 this was roughly corrected for based on a mean bed form celerity of $c_b = 2.9\,\mathrm{mm/s}$. This approach is sufficient for the present purpose, as it results in an upper bound of the error in the bed scans of the new method. An improved method of processing the line laser data to a regular 3-D matrix of subsequent bed topographies in the flume would be to extend the LOESS algorithm from 2-D to 3-D, to add the time dimension.

5. Conclusions

A line laser scanner offers the potential to replace existing bed form measurement techniques, such as those based on acoustics and single beam lasers. The highest accuracy of the new technique is achieved after applying both a background correction and a refraction correction. In moving bed experiments, the former is negligible compared to residual measurement error.

Flowing water conditions introduce a measuring error, especially for larger water depths. An increase in the number of missing values with increasing Froude number, established previously in the literature, is not confirmed in this study. Redundancy in the data allows to handle missing data when using an appropriate filter.

Satisfying results are obtained in a pilot experiment with a moving sand bed where dunes and bars develop. When a robust LOcally weighted regrESSion (LOESS) procedure is applied to interpolate the scattered data points void of outliers, an accurate, coherent bed topography is obtained. Bed forms can be tracked during the experiment and there is no need to disturb the flow while measuring, which is unavoidable when using acoustic techniques. When lightweight sediment is used, like polystyrene, dynamic similarity between the laboratory experiments and the field circumstances is achieved under low flow velocities, for which the line laser approach works best.

Appendix A: Mathematical Description of Mapping in Bins

The mapping of bed profile measurements in bins, as introduced in section 2.5, can be mathematically described as follows.

Bed level bins are defined as $[\tilde{z}_k, \tilde{z}_{k+1})$, where $\tilde{z}_k = z_0 + (k-1)\Delta z$, with $k = 1, 2, \ldots, k_{\max}+1$, z_0 a lower bound for the bed level and Δz the bin width. The probability p_k of a bed level value $z_i \in [\tilde{z}_k, \tilde{z}_{k+1})$ to be missed by the measurement device is

$$p_k = \frac{\#\{z_i \in [\tilde{z}_k, \tilde{z}_{k+1}) | z_i' = \mathrm{NaN}\}}{\#\{z_i \in [\tilde{z}_k, \tilde{z}_{k+1})\}},$$

where z_i are bed level values of the dry-bed profile and z_i' the corresponding measured values of the submerged profile.

Additional to the bed level bins, residual error bins are defined as $[\tilde{\epsilon}_m, \tilde{\epsilon}_{m+1})$, where $\tilde{\epsilon}_m = \epsilon_0 + (m-1)\Delta\epsilon$, with $m = 1, 2, \ldots, m_{\max}+1$, ϵ_0 a lower bound for the residual error and $\Delta\epsilon$ the bin width. The probability $p_{k,m}$ that a bed level value $z_i \in [\tilde{z}_k, \tilde{z}_{k+1})$ is measured with a residual error $\epsilon_i \in [\tilde{\epsilon}_m, \tilde{\epsilon}_{m+1})$ is

$$p_{k,m} = \frac{\#\{z_i \in [\tilde{z}_k, \tilde{z}_{k+1}) | \epsilon_i \in [\tilde{\epsilon}_m, \tilde{\epsilon}_{m+1})\}}{\#\{z_i \in [\tilde{z}_k, \tilde{z}_{k+1})\}}.$$

Appendix B: Fitting Parameters

The fitting parameters used for the background correction, a_i and b_i in equations (1) and (3), are given below. Due to re-installation and recalibration of the laser scanner for experiment 5, a different set of parameters is obtained there. For experiments 1 to 4 a longitudinal range of 7.5 cm ($x \in [1100; 1175]$ mm) is used to obtain $a_1 = -5.86\times10^{-6}\,\text{mm}^{-1}$, $a_2 = 5.04\times10^{-3}$ and $a_3 = -4.49\times10^{2}$ mm, and $b_1 = 9.99\times10^{-6}\,\text{mm}^{-1}$, $b_2 = -5.95\times10^{-3}$ and $b_3 = 8.40\times10^{-1}$ mm.

For experiment 5 a longitudinal range of 65 cm ($x \in [1050; 1685]$ mm) is used to obtain $a_1 = -7.83\times10^{-6}\,\text{mm}^{-1}$, $a_2 = 7.98\times10^{-3}$ and $a_3 = -6.10\times10^{2}$ mm, and $b_1 = -1.92\times10^{-6}\,\text{mm}^{-1}$, $b_2 = 1.55\times10^{-3}$ and $b_3 = -3.18\times10^{-1}$ mm.

Acknowledgments
This research is part of the research programme RiverCare, supported by the Dutch Technology Foundation STW, which is part of the Netherlands Organization for Scientific Research (NWO), and which is partly funded by the Ministry of Economic Affairs under grant number P12–14 (Perspective Programme). The data and scripts used in this study are publicly available online on http://hdl.handle.net/10411/YACJ6D. The numerical implementation of the LOESS algorithm in Matlab and C++ is open source and can be found on https://github.com/bartverm. The authors thank Associated Editor Charles Luce as well as Andrés Vargas-Luna and two anonymous reviewers for their comments, that helped improving the manuscript.

References

Abad, J. D., & Garcia, M. H. (2009). Experiments in a high-amplitude Kinoshita meandering channel: 2. Implications of bend orientation on bed morphodynamics. *Water Resources Research*, *45*, W02402. https://doi.org/10.1029/2008WR007017

Aberle, J., Henning, M., & Hentschel, B. (2009). Statistical analysis of bed form dynamics. In *Proceedings of the 33rd IAHR Congress, Vancouver, Canada* (pp. 1835–1841). Madrid, Spain: International Association for Hydro-Environmental Engineering & Research (IAHR).

Allen, J. R. L. (1984). *Sedimentary structures: their character and physical basis*. Amsterdam, the Netherlands: Elsevier.

Blom, A. (2008). Different approaches to handling vertical and streamwise sorting in modeling river morphodynamics. *Water Resources Research*, *44*, W03415. https://doi.org/10.1029/2006WR005474

Butler, J. B., Lane, S. N., Chandler, J. H., & Porfiri, E. (2002). Through-water close range digital photogrammetry in flume and field environments. *The Photogrammetric Record*, *17*(99), 419–439. https://doi.org/10.1111/0031-868X.00196

Cleveland, W. S. (1979). Robust local weighted regression and smoothing scatterplots. *Journal of American Statistical Association*, *74*(368), 829–836. https://doi.org/10.2307/2286407

Cleveland, W. S., & Devlin, S. J. (1988). Weighted regression: an approach to regresion analysis by local fitting. *Journal of American Statistical Association*, *83*(403), 596–610. https://doi.org/10.2307/2289282

di Risio, I. M., Lisi, B. G. M., P. & de Girolamo, (2010). Physical modeling of the cross-shore short-term evolution of protected and unprotected beach nourishments. *Ocean Engineering*, *37*, 777–789. https://doi.org/10.1016/j.oceaneng.2010.02.008

Freeze, B., Smolentsev, S., Morley, N., & Abdou, M. (2003). Characterization of the effect of Froude number on surface waves and heat transfer in inclined turbulent open channel water flows. *International Journal of Heat Mass Transfer*, *46*(20), 3765–3775. https://doi.org/10.1016/S0017-9310(03)00197-2

Friedrichs, M., & Graf, G. (2006). Description of a flume channel profilometry tool using laser line scans. *Aquatic Ecology*, *40*, 493–501. https://doi.org/10.1007/s10452-004-8057-0

Gaeuman, D., & Jacobson, R. B. (2007). Field assessment of alternative bed-load transport estimators. *Journal of Hydraulic. Engineering*, *133*(12), 1319–1328. https://doi.org/10.1061/(ASCE)0733-9429(2007)133:12(1319)

Guenther, G. C. (1985). *Airborne laser hydrography: System design and performance factors* (NOAA Professional Paper Series). Rockville, MD: National Oceanic Service 1, National Oceanic and Atmospheric Administration.

Gupta, H. V., Kling, H., Yilmaz, K. K., & Martinez, G. F. (2009). Decomposition of the mean squared error and NSE performance criteria: Implications for improving hydrological modelling. *Journal of Hydrology*, *377*, 80–91. https://doi.org/10.1016/j.jhydrol.2009.08.003

Henning, M., Hentschel, B., & Husener, T. (2009). Photogrammetric system for measurements and analysis of dune movement. In *Proceedings of the 33rd IAHR Congress, Vancouver, Canada* (pp. 4966–4972).

Hentschel, B. (2007). Hydraulische Flussmodelle mit beweglicher Sohle [In German]. *Mitteilungsblatt Der Bundesanstalt Für Wasserbau*, *90*, 25–46.

Huang, M. Y. F., Huang, A. Y. L., & Capart, H. (2010). Joint mapping of bed elevation and flow depth in microscale morphodynamics experiments. *Experiments in Fluids*, *49*, 1121–1134. https://doi.org/10.1007/s00348-010-0858-4

Hurther, D., Thorne, P. D., Bricault, M., Lemmin, U., & Barnoud, J. M. (2011). A multi-frequency Acoustic Concentration and Velocity Profiler (ACVP) for boundary layer measurements of fine-scale flow and sediment transport processes. *Coastal Engineering*, *58*, 594–605. https://doi.org/10.1016/j.coastaleng.2011.01.006

Krabill, W. B., Collins, J. G., Link, L. E., Swift, R. N., & Butler, M. L. (1984). Airborne laser topographic mapping results. *Photogrammetric Engineering and Remote Sensing*, *50*(6), 685–694.

Lane, S. N., Chandler, J. H., & Porfiri, K. (2001). Monitoring river channel and flume surface with digital photogrammetry. *Journal of Hydraulic Engineering*, *127*(10), 871–877. https://doi.org/10.1061/(ASCE)0733-9429(2001)127%3A10(871)

Lesser, G. R., Roelvink, J. A., van Kester, J. A. T. M., & Stelling, G. S. (2004). Development and validation of a three-dimensional morphological model. *Coastal Engineering*, *51*, 883–915. https://doi.org/10.1016/j.coastaleng.2004.07.014

Murphy, A. H. (1988). Skill scores based on the mean squared error and their relationships to the correlation coefficient. *Monthly Weather Review*, *116*, 2417–2424.

Muste, M., Baranya, S., Tsubaki, R., Kim, D., Ho, H., Tsai, H., & Law, D. (2016). Acoustic mapping velocimetry. *Water Resources Research*, *52*, 4132–4150. https://doi.org/10.1002/2015WR018354

Nabi, M., de Vriend, H. J., Mosselman, E., Sloff, C. J., & Shimizu, Y. (2013a). Detailed simulation of morphodynamics: 2. Sediment pickup, transport, and deposition. *Water Resources Research*, *49*, 4775–5791. https://doi.org/10.1002/wrcr.20303

Nabi, M., de Vriend, H. J., Mosselman, E., Sloff, C. J., & Shimizu, Y. (2013b). Detailed simulation of morphodynamics: 3. Ripples and dunes. *Water Resources Research*, *49*, 5930–5943. https://doi.org/10.1002/wrcr.20457

Naqshband, S., Ribberink, J., Hurther, D., & Hulscher, S. J. M. H. (2014). Bed load and suspended load contributions to migrating sand dunes in equilibrium. *Journal of Geophysical Research: Earth Surfaces*, *119*, 1043–1063. https://doi.org/10.1002/2013JF003043

Peña González, E., Sánchez-Tembleque Díaz-Pache, F., Pena Mosquera, L., & Puertas Agudo, J. (2007). Bidimensional measurement of an underwater sediment surface using a 3D-Scanner. *Optics & Laser Technology*, *39*, 481–489. https://doi.org/10.1016/j.optlastec.2005.11.007

Plant, N. G., Holland, K. T., & Puleo, J. A. (2002). Analysis of the scale of errors in nearshore bathymetric data. *Marine Geology*, *191*, 71–86. https://doi.org/10.1016/S0025-3227(02)00497-8

Seminara, G. (2010). Fluvial sedimentary patterns. *Annual Review of Fluid Mechanics*, *42*, 43–66. https://doi.org/10.1146/annurev-fluid-121108-145612

SICK. (2012). *Ranger E/D reference manual – MultiScan 3D camera with Gigabit Ethernet (E), 3D camera with Gigabit Ethernet (D)*. Waldkirch, Germany: SICK Sensor Intelligence.

Simpson, M. R., & Oltmann, R. N. (1993). Discharge-measurement system using an acoustic Doppler current profiler with applications to large rivers and estuaries. *United States Geological Survey Water-Supply Paper*, *2395*, 1–32.

Smart, G., Aberle, J., Duncan, M., & Walsh, J. (2004). Measurement and analysis of alluvial bed roughness. *Journal of Hydraulic Research*, *42*(3), 227–237. https://doi.org/10.1080/00221686.2004.9641191

Stefanon, L., Carniello, L., D'alpaos, A., & Lanzoni, S. (2010). Experimental analysis of tidal network growth and development. *Continental Shelf Research*, *30*, 950–962. https://doi.org/10.1016/j.csr.2009.08.018

Struiksma, N. (1985). Prediction of 2-D bed topography in rivers. *Journal of Hydraul. Engineering*, *111*(8), 1169–1182. https://doi.org/10.1061/(ASCE)0733-9429(1985)111%3A8(1169)

Tesser, G., Carniello, L., Defina, A., Lanzoni, S., Susin, F. M., & D'alpaos, L. (2007). Experimental analysis of tidal network growth and development. In Di Silvio, G. & Lanzoni, S. (Eds.), *Harmonizing the demands of art and nature in hydraulics: 32nd congress of IAHR*. Venice, Italy: CORILA.

Thorne, P., & Hanes, D. (2002). A review of acoustic measurement of small-scale sediment processes. *Continental Shelf Research*, *22*, 603–632. https://doi.org/10.1016/S0278-4343(01)00101-7

Vargas-Luna, A., Angel Escobar, J. A., Stierman, E. M. J., Gorte, B. G. H., & Uijttewaal, W. S. J. (2016). Measuring bathymetric evolution in mobile-bed laboratory flumes. In G. Constantinescu, M. Garcia, & D. Hanes (Eds.), *River Flow 2016* (pp. 146–147). Leiden, the Netherlands: CRC Press.

Vermeulen, B., Boersema, M. P., Hoitink, A. J. F., Sieben, J., Sloff, C. J., & van der Wal, M. (2014). River scale model of a training dam using lightweight granulates. *J. Hydro-Environmental Research*, *8*(2), 88–94. https://doi.org/10.1016/j.jher.2013.05.004

Visconti, F., Camporeale, C., & Ridolfi, L. (2010). Role of discharge variability on pseudomeandering channel morphodynamics: Results from laboratory experiments. *Journal of Geophysical Research*, *115*, F04042. https://doi.org/10.1029/2010JF001742

Visconti, F., Stefanon, L., Camporeale, C., Susin, F., Ridolfi, L., & Lanzoni, S. (2012). Bed evolution measurement with flowing water in morphodynamics experiments. *Earth Surface Processes and Landforms*, *37*, 818–827. https://doi.org/10.1002/esp.3200

Yeh, P.-H., Chang, K.-A., Henriksen, J., Edge, B., Chang, P., Silver, A., & Vargas, A. (2009). Large-scale laboratory experiment on erosion of sand beds by moving circular vertical jets. *Ocean Engineering*, *36*, 248–255. https://doi.org/10.1016/j.oceaneng.2008.11.006